geosciences

MDPI

Article

High-Silica Lava Morphology at Ocean Spreading Ridges: Machine-Learning Seafloor Classification at Alarcon Rise

Christina H. Maschmeyer [1,†], Scott M. White [1,*], Brian M. Dreyer [2] and David A. Clague [3]

[1] School of the Earth, Ocean and Environment, University of South Carolina, Columbia, SC 29208, USA; c.maschmeyer@fugro.com
[2] Institute of Marine Sciences, University of California, Santa Cruz, CA 95064, USA; bdreyer@ucsc.edu
[3] Monterey Bay Aquarium Research Institute, Moss Landing, CA 95039, USA; clague@mbari.org
* Correspondence: swhite@geol.sc.edu
† Present address: Fugro USA Marine, Inc. Geoconsulting Exploration, 6100 Hillcroft Ave, Houston, TX 77081, USA.

Received: 31 March 2019; Accepted: 28 May 2019; Published: 1 June 2019

Abstract: The oceanic crust consists mostly of basalt, but more evolved compositions may be far more common than previously thought. To aid in distinguishing rhyolite from basaltic lava and help guide sampling and understand spatial distribution, we constructed a classifier using neural networks and fuzzy inference to recognize rhyolite from its lava morphology in sonar data. The Alarcon Rise is ideal to study the relationship between lava flow morphology and composition, because it exhibits a full range of lava compositions in a well-mapped ocean ridge segment. This study shows that the most dramatic geomorphic threshold in submarine lava separates rhyolitic lava from lower-silica compositions. Extremely viscous rhyolite erupts as jagged lobes and lava branches in submarine environments. An automated classification of sonar data is a useful first-order tool to differentiate submarine rhyolite flows from widespread basalts, yielding insights into eruption, emplacement, and architecture of the ocean crust.

Keywords: seafloor classification; lava morphology; remote sensing; machine learning; fuzzy logic; oceanic spreading ridge

1. Introduction

Seafloor produced at spreading ridges consists mostly of basaltic lava; however, more evolved rock compositions are not as rare as previously believed. In fact, non-basaltic compositions might often be associated with ridge axis discontinuities [1–4] and thereby constitute a significant fraction of oceanic crust. The difficulty of locating these outcrops of non-basaltic rock types during the limited time and distance of deep-sea dives motivates this study to investigate alternate methods of prospecting for high-silica submarine lava types. Alarcon Rise, in the Gulf of California, is a unique ridge segment with lava flows with mafic, intermediate, and felsic compositions (Figure 1). The goal of this study was to determine whether morphology can be used to identify submarine lava flows of different compositions.

Basalt submarine lava morphologies are mainly controlled by lava effusion rate [5,6] sheet to pillow flows [6–12]. Lava containing more silica is typically described as large pillows for andesite or dacite composition (e.g., [13,14]) (Figure 2). In 2012, the first spreading ridge rhyolites were discovered along a faulted ridge and breccia-covered mound in Alarcon Basin [15].

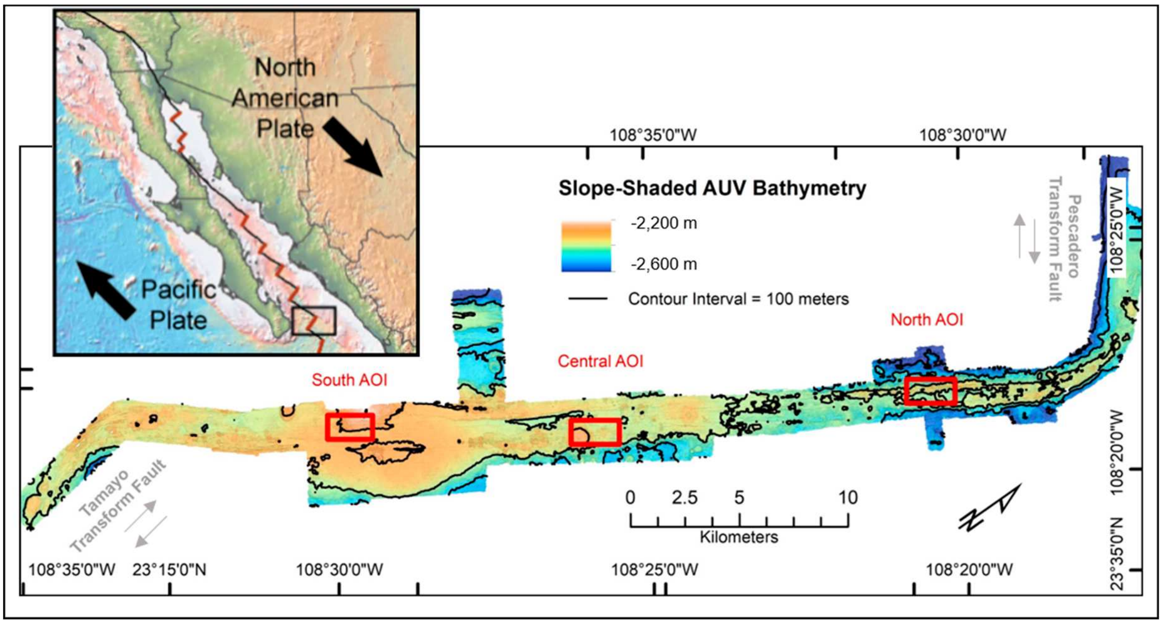

Figure 1. The Alarcon Rise is the south en-echelon ocean spreading ridge in the Gulf of California (black box in inset). Note that the map is oriented with north toward the upper right, and coordinate tics are spaced at 5 arc-minute intervals. The entire area of autonomous underwater vehicle (AUV) bathymetry at the Alarcon Rise is our study area, and three Area of Interest (AOI) locations (red boxes) referred to in this study are the volcanic shield (South AOI), volcanic cone (Central AOI), and high-silica ridge (North AOI).

We anticipated differences in lava flow morphologies would result from lava composition changes just as increasing viscosity can change basaltic lava flows from sheet to pillow flow [8,16]. Evidence from the visual geologic mapping suggests that rhyolites display a morphology distinct from that of other lava compositions, suggesting that an automated classifier could identify that morphologic threshold in meter-scale resolution bathymetry data. Here, we investigated geomorphic characteristics inherent to rhyolitic submarine lava flows at spreading ridges. To aid in distinguishing a geomorphic fingerprint for rhyolitic lava from that for basaltic lava, we constructed an artificial intelligence classifier.

Rhyolitic submarine domes and lava morphology have been described previously in volcanic arcs [17,18], fore-arcs [19], and convergent continental margins [20,21] at Alarcon Rise was recovered from a 500 m-diameter dome protruding from a 9 km-long ridge (Figure 2); we wanted to determine geomorphic differences in lava flows as their silica composition changes. Chadwick et al. [22] noted that multibeam bathymetry gridded at 1 m provides sufficient resolution to directly measure dikes, faults, and lava flows. To study individual rhyolitic lava flows rather than volcanic edifice properties at Alarcon Rise, we utilized the same type of 1 m gridded multibeam bathymetry from which rhyolitic flows can be delineated by texture.

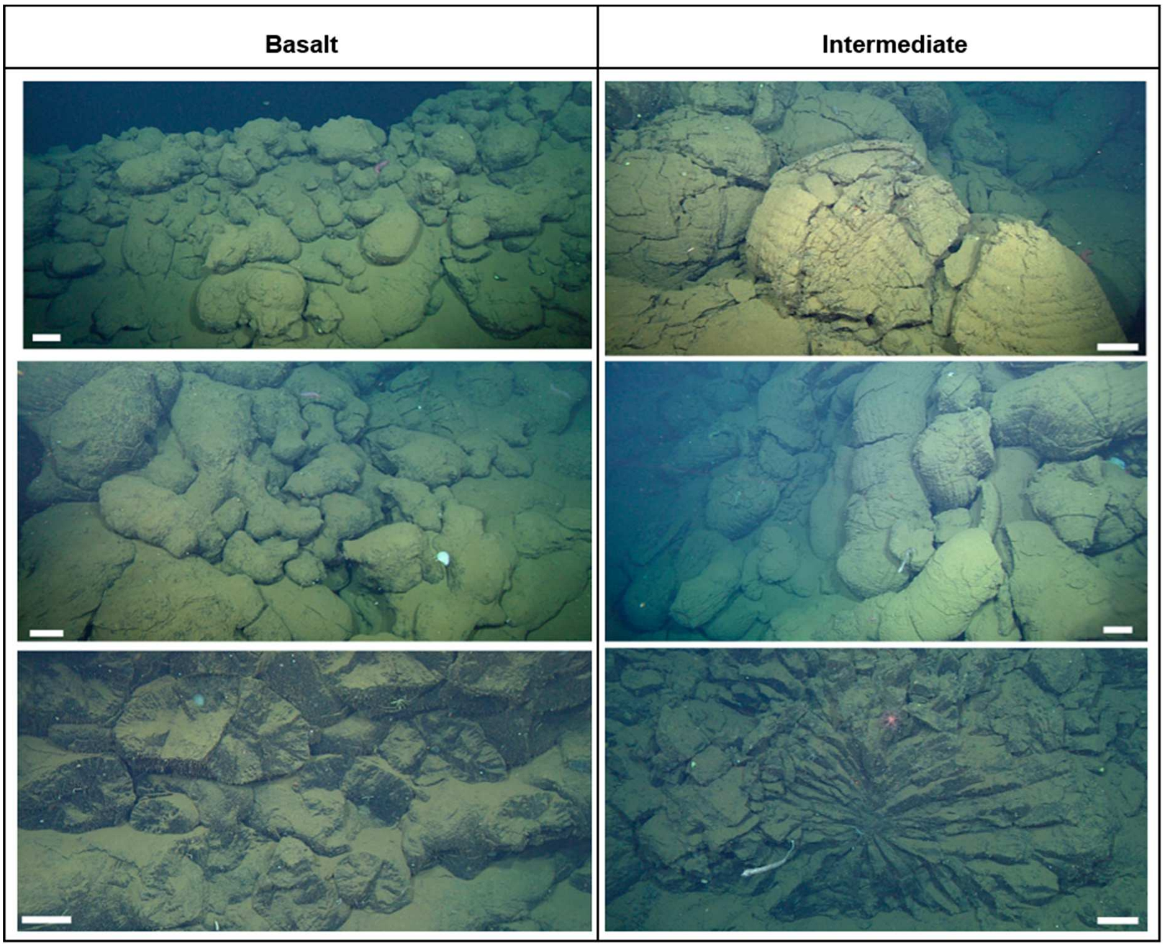

Figure 2. Comparison of the scale of intermediate and basaltic pillows in Remotely Operated Vehicle (ROV) *Ricketts* photographs. The white line represents 1 m for each image. Basalt pillows have average diameters of ~1 m, whereas intermediate pillows consistently have much larger diameters >1 m; intermediate pillows also have roughly striated surfaces and extreme radial jointing.

2. Data Collection

MBARI completed mapping and sampling expeditions to the Alarcon Rise in 2012 and 2015. MBARI mapped approximately 165 km^2 of the Alarcon Rise using autonomous underwater vehicle (AUV) *D Allan B*. Data with a 1 m lateral and 0.1 m vertical resolution were collected by a Reson 7125 200 kHz multibeam sonar system at 60–90 m above the seafloor in 2015 to map the spreading ridge; raw data are available at doi:10.1594/IEDA/324367 [23]. MBARI processed the raw multibeam sonar data in MB-System. The data were processed following the procedures in Caress et al. [24] for removing bad navigation fixes, matching features on adjacent and crossing tracklines to tighten the relative navigation and manual editing to remove sonar artifacts. Because the classification is resolution-dependent, higher resolution grids would be more sensitive to lava morphology expressed at the meter scale. Gridding at finer intervals <1.0m introduces stochastic noise which degrades all of the derived-bathy data used in the classifications. We used the resulting 1 m gridded bathymetric data in this study to minimize noise and as appropriate to the beam sounding density of these data [15,23]. Resolution provided by 1 m gridded data retains the scale of roughness to distinguish lava megapillows (>1 m diameter) and jagged flows suspected to represent higher-silica lava from smoother flows typical of basalts.

MBARI conducted two sampling expeditions to the Alarcon Rise on the R/V *Western Flyer*. Three hundred and sixty-two lava flow samples were collected along the spreading ridge. ROV *Doc Ricketts* collected 314 in situ rock samples, and R/V *Western Flyer* collected 27 samples of glass chips and rock fragments by rock corer. Subsequent MBARI cruises following the two main sampling expeditions retrieved 21 additional lava samples that we used in this study. Samples collected in 2012 by ROV *Doc Ricketts* have a geographic uncertainty of ~20 m, [15], and rock corer samples of ~10 m.

Following the sampling expeditions, Clague et al. [15] analyzed each sample for geochemical composition. Volcanic glass from most samples was basalt with MgO of 6.0–8.6 wt%; however, some samples collected from north Alarcon Rise (north AOI, Figure 1) had low MgO wt% and SiO_2 57–78 wt%, corresponding to intermediate-to-felsic compositions [15]. Classification of rock type follows Clague et al. [15], with rhyolites containing SiO_2 74–78 wt.%.

3. Ridge Description

The Alarcon Rise is an intermediate spreading ridge with a full-spreading rate of ~50 mm/a [25]. The geomorphology of the Alarcon Rise, like that of other intermediate-rate (40–80 mm/a) ridges, contains regions similar to faster and slower spreading ridges [9]. We divided Alarcon Rise into segments north and south of 23°36′ N based on kilometer-scale geomorphic differences and spreading axis continuity (Figure 3), following Clague et al. [15]. Sheet flows form broad low-relief lava shields over the south segment of the Alarcon Rise and a ~700 m-diameter pillow mound. The central portion of the Alarcon Rise exhibits a flat-topped volcanic cone with a ~700 m diameter, and smaller pillow mounds (100–200 m diameters) and sheet flows also cover the central region. All samples collected from the south and central sections of the Alarcon Rise were basaltic.

The north segment of the Alarcon Rise resembles slow-spreading ridges with faults and fissures 400–600 m long and axial volcanic ridges (e.g., [26]). A ~9 km long axial ridge separates the north segment to the west of the ridge into large (>1 m diameter) pillows with deep (>1 cm) striations giving the bathymetry of this area a hummocky texture (Figure 2). These are all evolved lava compositions [15]. To the east of the ridge, quasi-circular, smooth pillow mounds and smooth sheet flows dominate.

A ~500 m diameter rhyolite dome protrudes from the axial ridge (Figure 4). The rhyolite dome has a jagged surface composed of angular, blocky lava flows and breccia (Figure 5). Similar observations regarding submarine rhyolite domes constructed from elongated brecciated lobes >1 m in diameter and angular blocks of lava have been made in arc settings [18,21]. Rhyolite flows likely formed as autobrecciated, jagged, or "toothpaste" morphology.

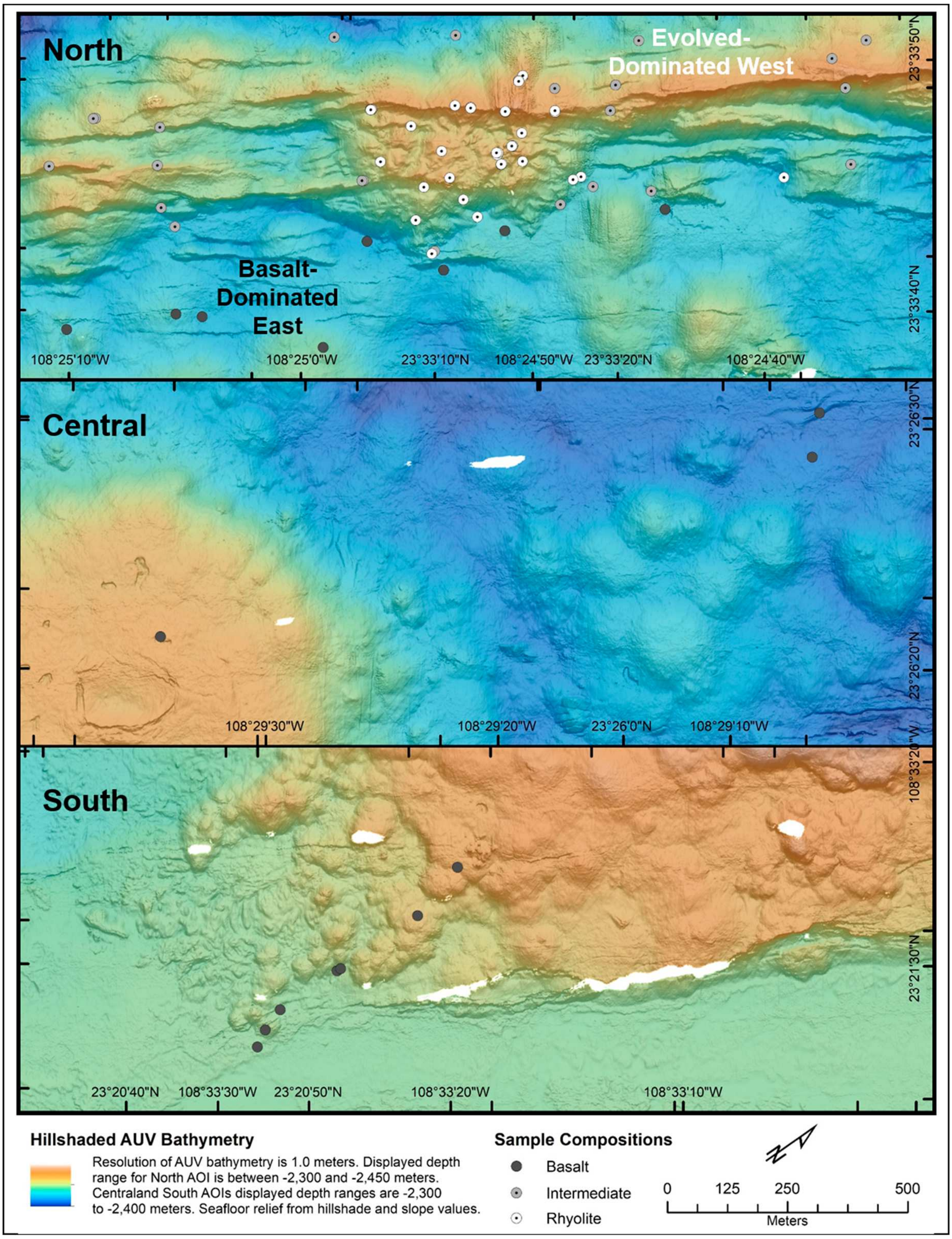

Figure 3. Examples of the distinct geomorphic provinces at the Alarcon Rise from Figure 1. Samples with basalts on mounds on the east and rhyolites cropping out on the ridge to the west were collected in the north AOI (top panel), which shows the rhyolitic dome and part of a 9 km-long ridge. The central AOI is dominated by a 700 m-diameter volcanic cone in the lower left of the map area shown (middle panel). The south AOI is dominated by a hummocky lava shield to the east side of the spreading axis (bottom panel).

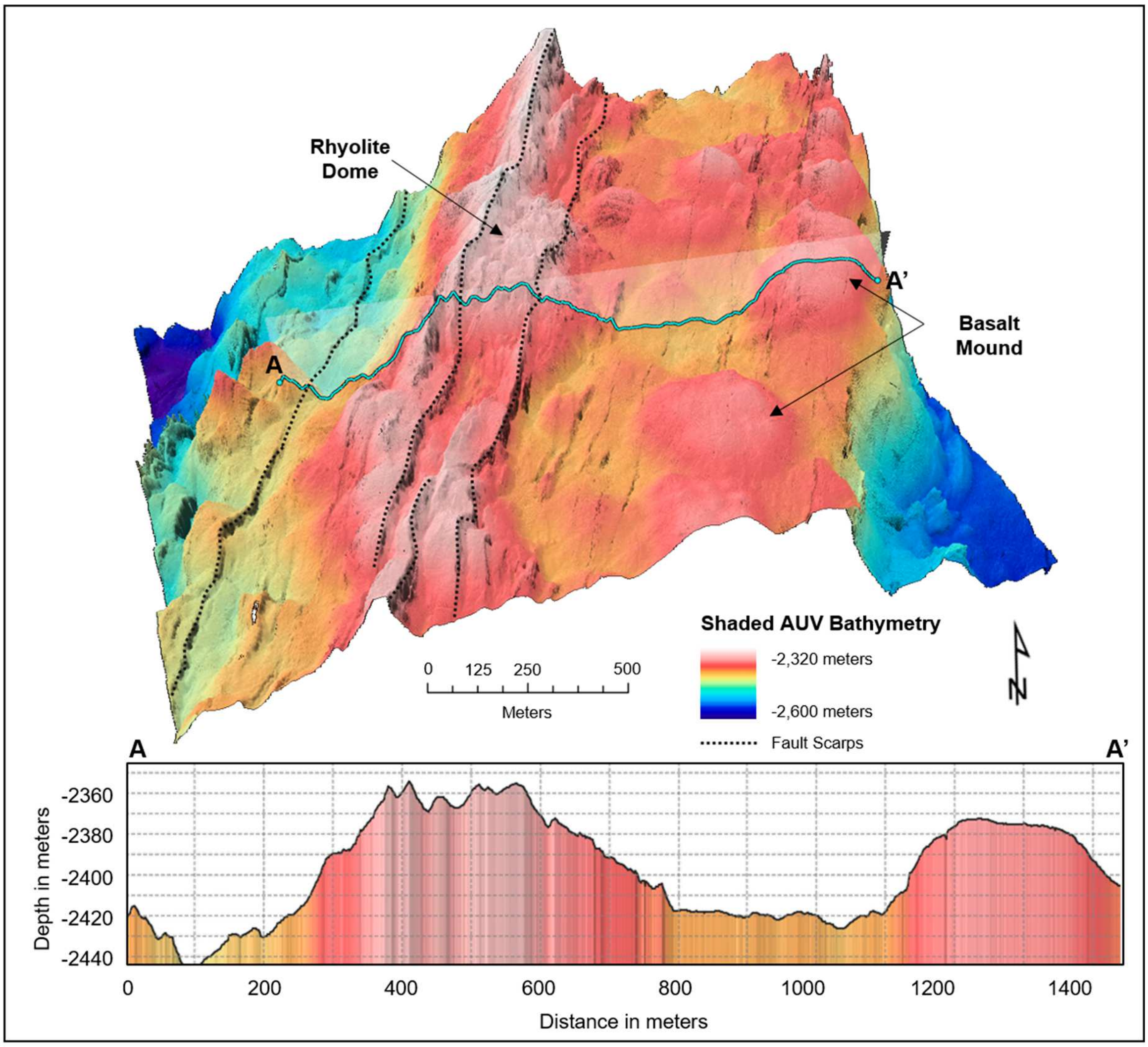

Figure 4. 3D perspective of the high-silica region in the north AOI at 3× vertical exaggeration. The rhyolite dome extrudes from a central ridge that separates the high-silica zone to the west. Lava on the rhyolite dome create a jagged texture of the seafloor. In contrast, quasi-circular basalt mounds have smoother surfaces in the AUV bathymetry.

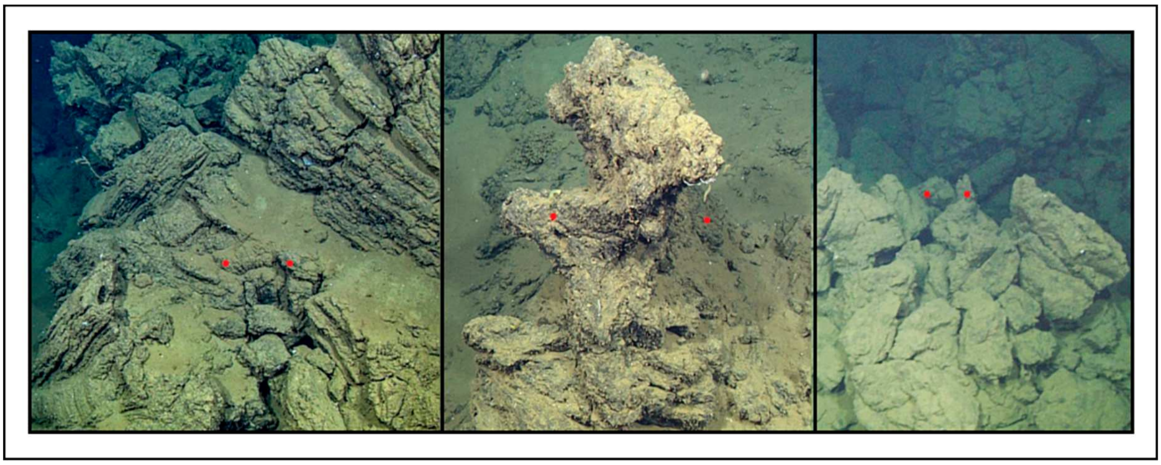

Figure 5. Examples of rhyolitic lava flows in ROV *Doc Ricketts* images. Laser spacing (red dots) is 70 cm. Rhyolitic flows can be blocky and angular with deep corrugation (left), form branches with jagged nodules (middle), or sometimes resembles blocky breccia (right).

4. Lava Morphology Characteristics of Basalt to Rhyolite

Submarine flow morphologies of evolved lava compositions have been recorded at some propagating ridge tips, overlapping spreading centers, ridge-transform intersections, and supra-subduction spreading [1–4,27,28]. Andesites and dacites formed elongated, large (<1 m diameter) pillow lavas with deep striations at the Galapagos Spreading Center and the eastern limb of 9° N East Pacific Rise overlapping spreading center [13]. Where the Juan de Fuca Ridge propagates past the Blanco Transform Zone, andesites and dacites were recovered from two small domes 200–500 m in diameter [14].

To determine if geomorphic characteristics can be used to classify submarine rhyolite flows and basalt flows at the Alarcon Rise, we took quantitative measurements of the geomorphology at type locations chosen from the bathymetry and rock samples. The rough texture, abundance of hummocks, and jagged surface of the rhyolite dome is visually distinct from the smooth texture, low density of local peaks and uniform surface of basalt mounds. To quantify these differences for machine-learning classification, we derived three datasets from the original 1 m-resolution bathymetry: maximum slope, bathymetric position index (BPI), and slope range. However, all the evaluated variables are known to have issues for being input-resolution-dependent. The evaluation of results obtained using different input resolutions is a known issue, discussed further in Section 9.

Classification variables were chosen on the basis of a combination of their ability to quantify the lava morphology at the scale of the bathymetry data and an iterative process where combinations of variables were tested to remove redundancy and lower classification uncertainty. Initially, we considered many variables for inclusion in the classification scheme including depth, aspect, slope, and rugosity indices. Principal component analysis (PCA) analysis indicated these variables were highly correlated with slope or BPI. We discarded the most redundant variables and retained the three described here.

Although we focused on lava flow scale with pixel-based classification, we integrated information at both scales with our neighborhood size of slope, BPI, and slope range. Depth and aspect biased the classifier towards specific depths and azimuth directions, respectively, and the rugosity index that most effectively distinguished local and ridge-scale roughness was BPI.

Slope is thought to have a profound effect on lava morphology, and previous classifications found it useful [5,29–32]. We calculated slope at a 1 m grid spacing using Horn's method to find the maximum slope in a 3×3 m moving window where the ratio of the rate of change of the surface in the horizontal to the vertical direction determined the slope [33]. Faults appeared as linear, near-vertical features in multibeam sonar bathymetry (Figure 6). To reduce the influence of faulting on the slope values of lava flows, we removed all grid cells with slope values above >45°. Setting this threshold also removed many of the sonar artifacts. We used >45° slope to mask faults in the original bathymetry before deriving other datasets. We observed that most basaltic lava flows formed slopes $< 20°$, whereas the majority of rhyolitic flows had slopes 20–40° (Figure 6).

To capture the pattern of small hummocks of high-silica lava flows at the rhyolite dome and west of the north ridge, we calculated the BPI. The BPI is the vertical difference between a depth of a point on the seafloor and the mean depth of a user-specified region [34]. We calculated BPI over a 0.5 km moving window chosen to capture vertical variation at a scale large enough to distinguish the rhyolite dome (diameter ~500 m) as the largest feature of interest (Figure 7). Basalt generally does not form local peaks or high slopes, indicated by BPI values near 0. Rhyolitic flows often build multi-tiered structures of individual hummocks, reflected by the bimodal distribution of BPI values (Figure 7, bottom panel).

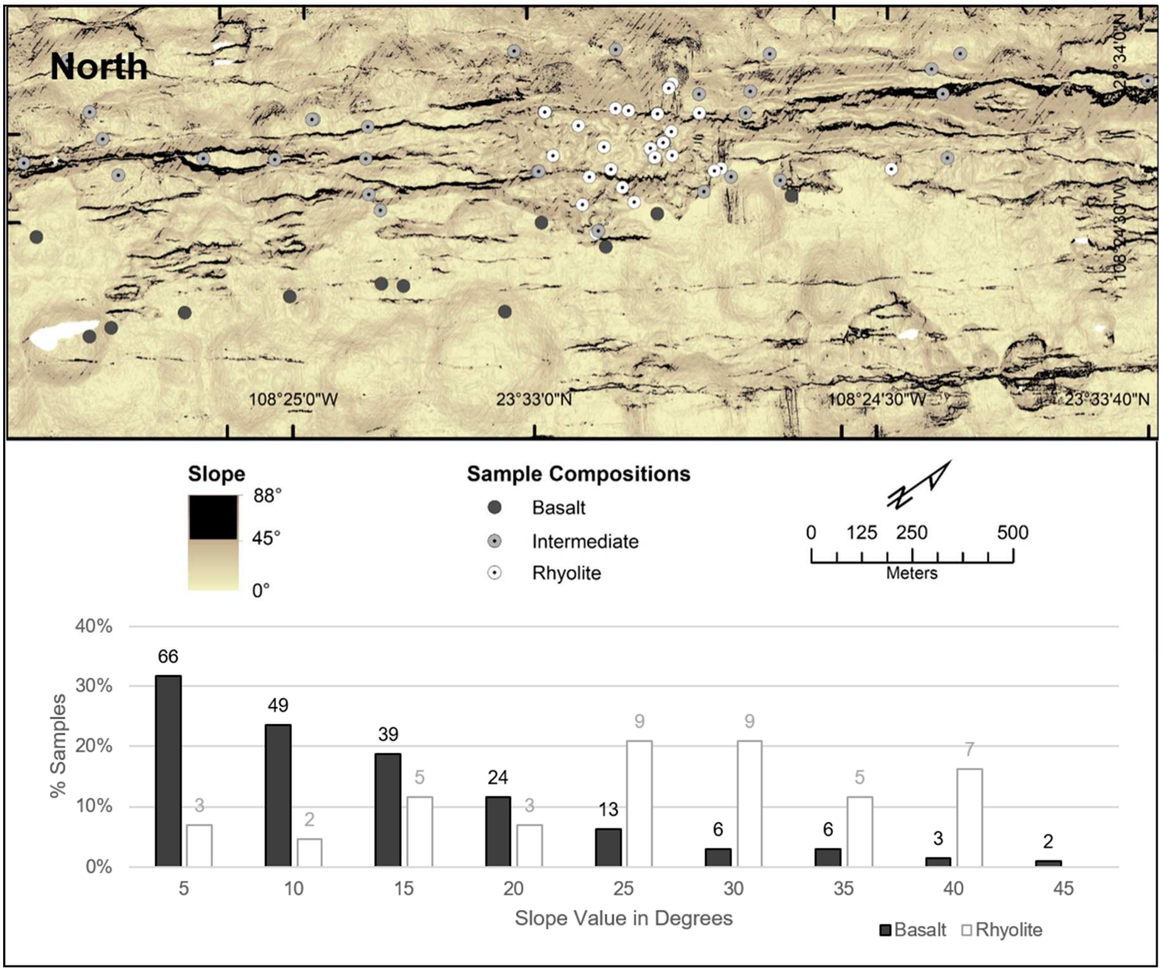

Figure 6. Slope (top panel) showing that rhyolites are associated with steep slopes, along with many intermediate compositions. Slope values >45° were only associated with faults and removed from the dataset used for lava morphology classification.

Slope profiles taken at the rhyolite dome and basalt mounds indicated that rhyolitic lava had not only higher slopes than basalts but also a distinctive range of slope values (Figure 8). A 10 × 10 m neighborhood, roughly 3 times the size of the moving window used for the slope calculation, was chosen to be larger than large-pillow size but also as small as possible. Rhyolite flows typically show a larger range of slope values than basalt flows. Slope range of more than 20° captures the jagged nature of rhyolite at the 10 m scale. Most basaltic lava flows form smooth-surfaced volcanic features, indicated by a slope range of <10°. We calculated the range of slope in 10 m blocks using a directional filter parallel to the spreading ridge axis. Directional filtering combined with the 45° threshold limited the influence by extensional faulting. A principal component analysis confirmed that slope and slope range datasets were not redundant, as one would expect from the different window sizes.

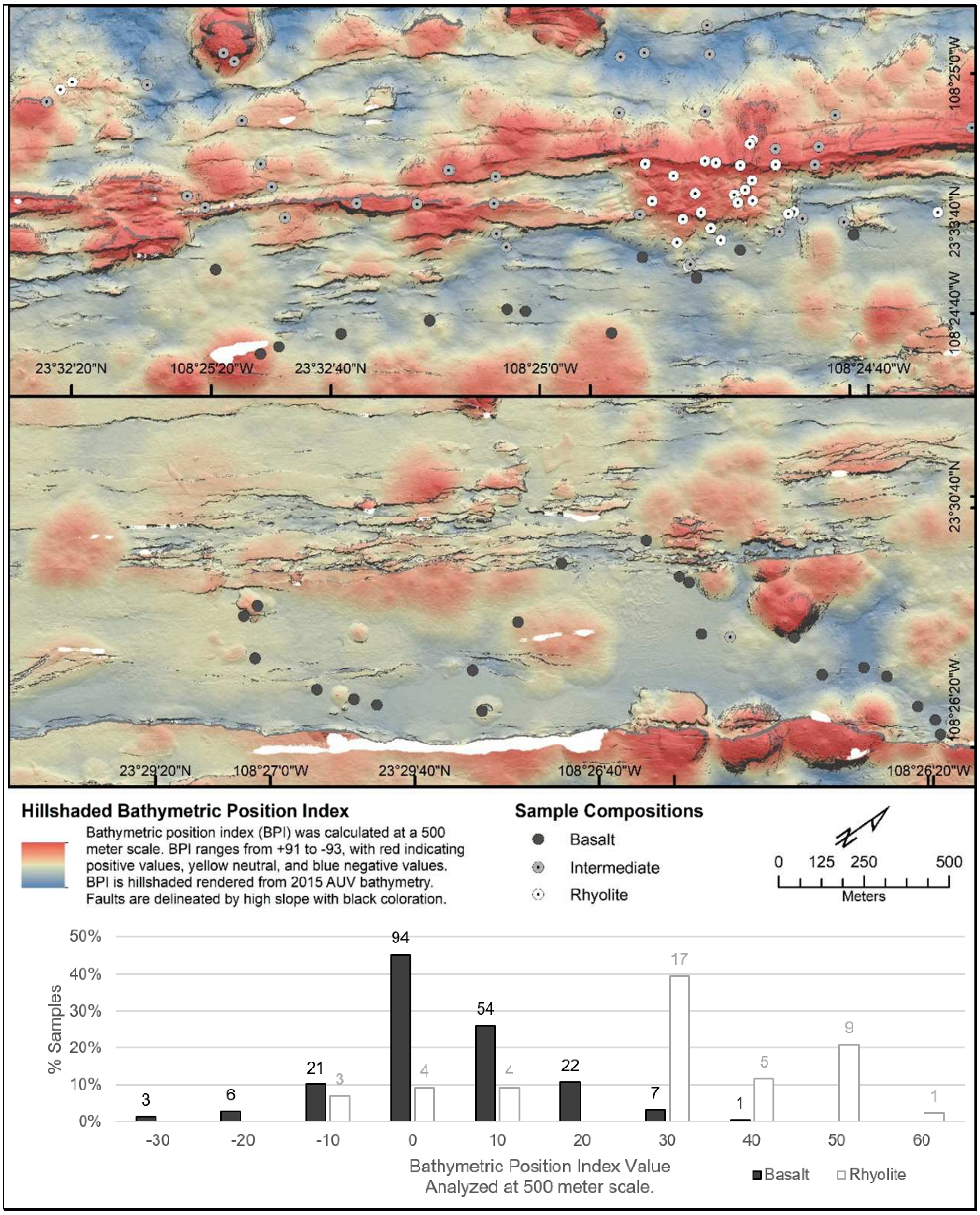

Figure 7. Bathymetric position index (BPI) values at the 0.5 km scale at the Alarcon Rise for two examples within the North AOI (top panel) and to the south of that region (middle panel) to illustrate a mainly basaltic flows and the rhyolitic area. Basalt samples from flat terrain about a zero value with a few basalts collected on isolated pillow mounds resulting in a high BPI value (bottom panel). Most rhyolitic samples had high BPI values.

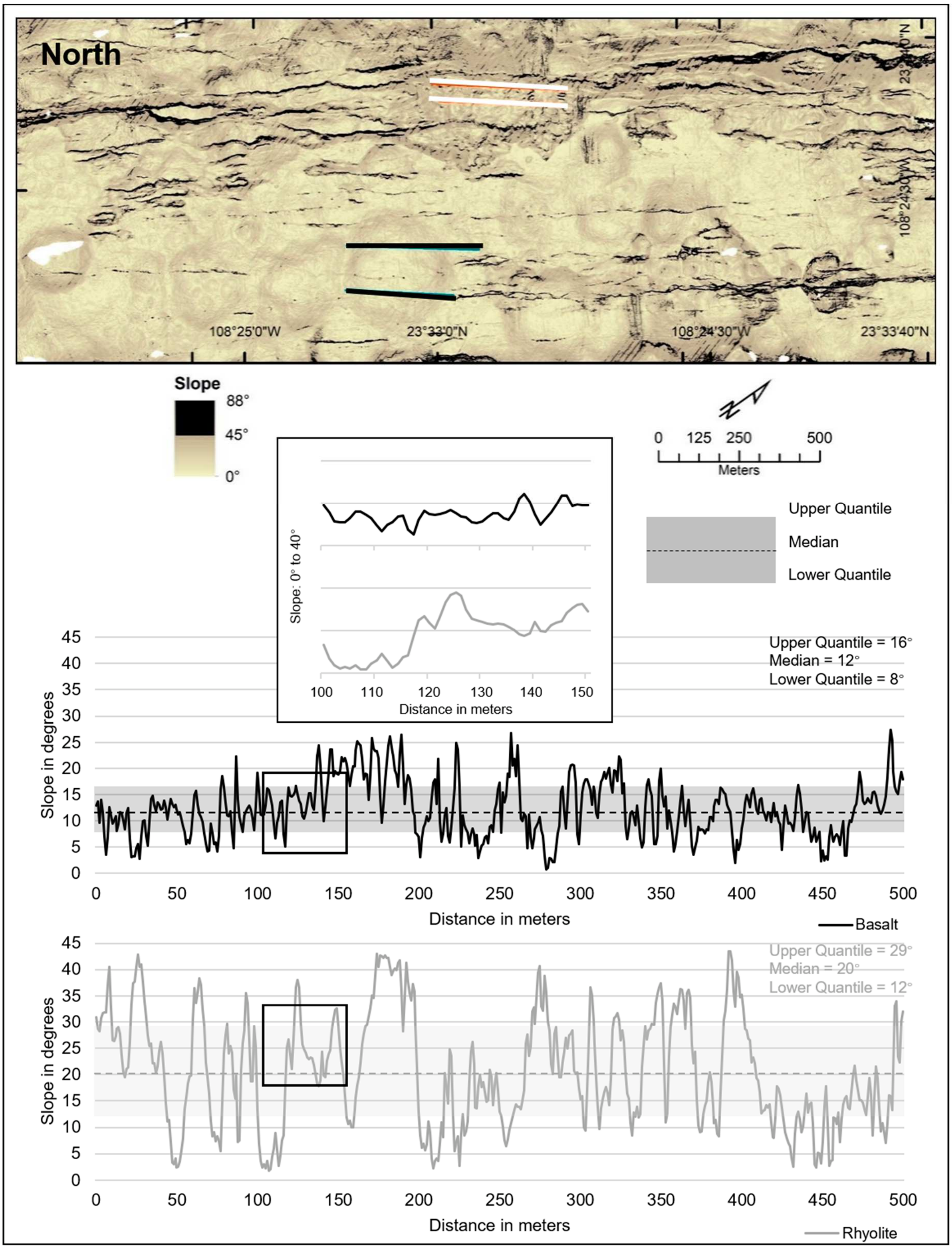

Figure 8. The top panel shows the locations of the slope profiles at the rhyolite dome (white lines) and on a basalt mound (black lines) shown in the lower two panels. The slope profiles were taken parallel to the axis to diminish any residual effects of faulting. Slope values for rhyolitic lava flows are consistently higher than those of basalt pillow mounds. Slope ranges of rhyolite flows are also greater than those of basaltic flows.

5. Lava Morphology Classification Method

Here, we attempted a classification of basalts and rhyolites at Alarcon Rise using an adaptive neuro-fuzzy inference system (ANFIS) that has proven effective at distinguishing lava morphology using sonar data [32]. Artificial intelligence classifiers are powerful tools for mapping submarine volcanic features (e.g., [31,35–37]). ANFIS combines the processing power of an artificial neural network with fuzzy logic [38]. Neural networks mimic the human nervous system by using processing nodes (neurons) connected to one another via weighted paths. Fuzzy classification is particularly appropriate because it models the natural continuum of lava composition expressed through the changing geomorphology of submarine lava flows. Unlike hard classification systems that assume discrete boundaries between homogenous classes, ANFIS uses fuzzy logic to assign a continual grade to heterogeneous classes with indistinct boundaries [38,39]. This is the first study to apply fuzzy inference classification to classify seafloor lava compositions. Limitations of the current methods are that categorical groups designed by the classifier give very little sense of the uncertainty of the classification beyond standard accuracy assessment.

The ANFIS classifier was constructed in MatLab using the Fuzzy Logic Toolbox and syntax library. Bathymetric data rasters were converted to xyz point tables for each pixel in the raster containing geospatial coordinates and the value associated with each input (slope, BPI, or slope range). After loading the ANFIS library in Matlab, a training cycle was initiated to find the best assignment functions of predetermined classes (basalt and rhyolite). The ANFIS learning process involves three steps. First, the system constructs if-then rules from the training data provided. Second, membership distribution functions are assigned to fit the value of the pixels in the classes represented by the training data. Third, ANFIS creates the neural-network structure that stores the rules. This process is repeated in each training cycle, when the weights of paths between each node are adjusted to minimize the error between the training input values and the classified output values.

Once the smallest class assignment uncertainty was reached during training, the structure of the classification was saved as a Fuzzy Inference System (FIS). Data to be classified were then loaded to the FIS. The rules created during the training cycle were applied in Matlab, and each row on the matrix (representing a different spatial point) was assigned a probability of belonging to a signature class.

We trained ANFIS to recognize basalt and rhyolite from slope, BPI, and slope range values extracted at ground-referenced locations of rock samples comprising the training data (Figure 9). ANFIS created three membership functions to distinguish between the classes. The iterative learning process inherent to the design of ANFIS determines the number of membership functions. ANFIS optimizes the classification by selecting the lowest number possible of membership functions to produce the lowest classification uncertainty from the training cycle. One hundred and fifty-six basalt and 30 rhyolite samples were used to train the classifier (data available in Clague et al. [15] as supplementary tables). The learning phase required <10,000 iterations to achieve a training accuracy of 84%. We reserved data from 52 basalt, 13 rhyolite, and 79 intermediate samples to test the accuracy of our classification.

To classify lava flows at the Alarcon Rise, we divided the 165 km^2 of 1 m bathymetry into point grids of non-overlapping 2 × 2 pixels representing 4 m^2 of seafloor as multibeam echosounder survey data (Figure 9). The pixel values for slope, BPI, and slope range at the geographic location of each point were extracted along the entire Alarcon Rise. ANFIS classified each point on the basis of the knowledge base developed during the learning phase. We then converted the classified point grids to a classified raster data. Each pixel represented 4 m^2 of the spreading ridge. We smoothed the classification to diminish the effect of speckle with a 10 m majority filter that selected for the most common value to replace the assumed mis-classified outlier value. The classified zones were then defined using the boundary clean and nibble functions in the Spatial Analyst toolbox of ArcGIS 10.4 to make cohesive classified regions more prominent on the map.

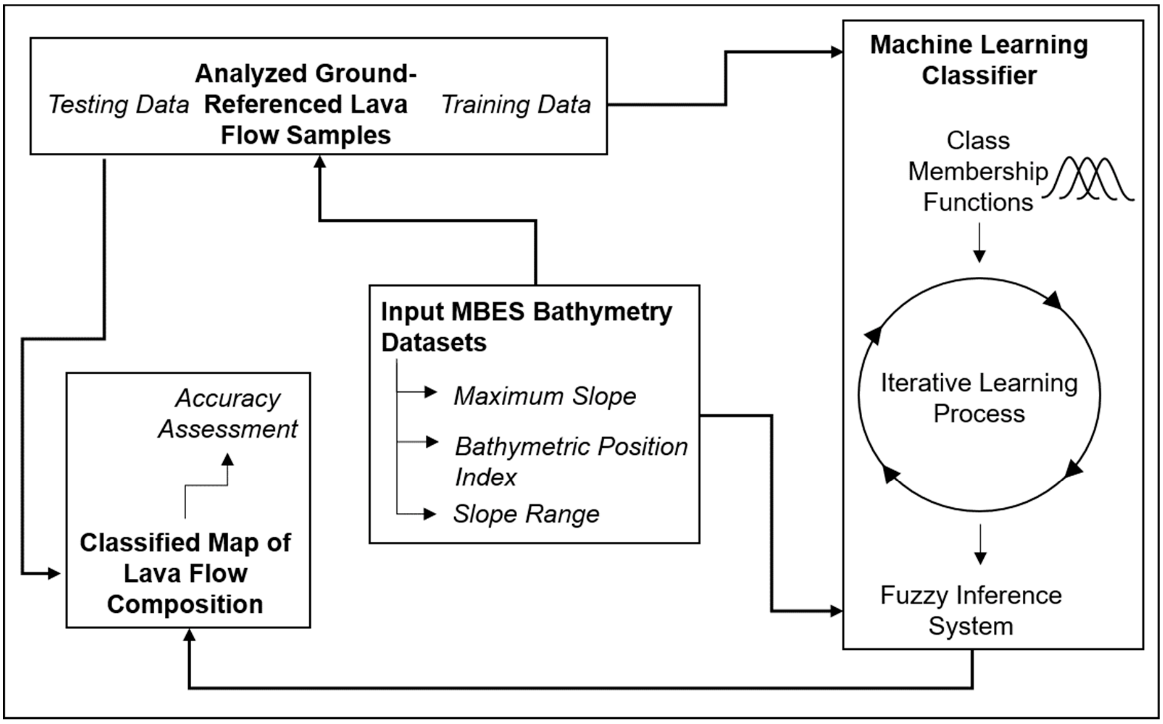

Figure 9. Adaptive neuro-fuzzy inference system (ANFIS) classification workflow. Ground-reference samples of basalt or rhyolite are divided into independent testing and training datasets. Slope, BPI at the 500 m scale, and slope range values are extracted at the training datapoints. The classifier then creates membership functions and classification rules. The resulting fuzzy inference system (FIS) classifies every 4 m^2 of seafloor with a probabilistic estimate of belonging to a rhyolite or basalt class. We tested the accuracy of our classification by reserving the testing data and comparing the sample composition to the ANFIS-assigned class.

6. Training Data Selection

To classify lava composition on the basis of the geomorphic attributes of submarine lava flows, we needed to compile a robust dataset of ground-referenced samples. Training data are ground-referenced points with known lava compositions that provide representative examples of each class. The samples collected in 2012 and 2015 limited our training data selection and spatial distribution. Only 45 samples were rhyolite, less than the minimum recommendation made by Congalton [40] of 50 samples per class. We rejected samples that were located at bathymetric data gaps, faults, or sedimentary basins off axis. If more than one sample of the same composition was collected at a given location for a certain lava flow, only one of the samples was used to help mitigate the effects of clustering common in deep-sea sample collection. These criteria further reduced to 2 rhyolitic, 5 intermediate, and 22 basaltic samples from the ground-referenced dataset suitable for training the classifier. We designated 75% of the remaining samples as training data and reserved 25% for accuracy assessment that were somewhat randomly selected but still spatially distributed.

7. Accuracy Analysis

A full and robust accuracy analysis was precluded by the small number and clustered spatial distribution of samples available for the classification of rhyolitic lava flows on the seafloor. Error and accuracy matrices provide a quantitative assessment of classification performance when remotely sensed categorical data meet the requirements outlined in Congalton [40]. To better evaluate the reliability of accuracy assessment metrics in light of the limitations imposed by the relatively small number of ground-reference samples—a typical situation in deep-ocean studies—we present two scenarios to gain an understanding of how consistently ANFIS performed as the testing datasets changed for each scenario or whether slight changes in the assessment data might affect the accuracy assessment. We present normalized accuracy matrices for each scenario to diminish the effect of sampling bias [40], such as bias from the paucity of rhyolitic samples.

We calculated three accuracy metrics for each scenario. Overall accuracy is the number of samples correctly classified divided by the number of samples. Producer's accuracy (PA) is a descriptive statistic that indicates omission error when a pixel is excluded from the correct class by misclassification. User's accuracy (UA) accounts for errors of commission when a point is assigned to the incorrect class and reflects the likelihood that a user would find that any given pixel on the map is misclassified. Kappa coefficient measures agreement from 0 (no agreement) to 1 (complete agreement) between the ground-referenced data and the classified map [41]. Unlike overall accuracy, Kappa coefficients adjust for chance agreement between classification and testing data.

Scenario 1 compared 52 basaltic samples to 13 rhyolite samples (Table 1). Classification performed better for basaltic morphology than rhyolite morphology; 38% of rhyolite samples were classified correctly (Table 1). UA in Scenario 2 increased to 100% (Table 2) by removing two basalt testing samples that were collected on talus slopes.

Table 1. Normalized accuracy assessment. PA: producer's accuracy, UA: user's accuracy.

	Ground Reference Classes				
ANFIS Classes	**Basalt**	**Rhyolite**	**Total Possible**	**PA**	**UA**
Basalt	0.78	0.19	0.97	78%	81%
Rhyolite	0.22	0.81	1.03	81%	79%
Total	1.0	1.0	2		
Overall Accuracy	80%				
Kappa Value	0.60				

Overall accuracy remained consistent in the range of 80–95%, and Kappa was in the range of 0.60–0.90. Testing points were collected from both on and off the rhyolite dome, where distinctive jagged rhyolite flows were evident, and four samples were classified as rhyolite. Three points were collected along the flanks of the dome, and six were located outside the rhyolite dome (Figure 10). Our testing data contained only one point outside the dome as rhyolite, which ANFIS classified correctly. In Scenario 1 (Table 1), the value of the Kappa coefficient indicated moderate-substantial agreement between the classified map and the ground-reference data, and Scenario 2 was 0.90 (Table 2), indicating nearly perfect agreement [41].

Table 2. Normalized accuracy assessment of data without basaltic talus.

	Ground Reference Classes				
ANFIS Classes	**Basalt**	**Rhyolite**	**Total Possible**	**PA**	**UA**
Basalt	1.0	0.1	1.1	100%	91%
Rhyolite	0	0.9	0.9	90%	100%
Total	1	1	2		
Overall Accuracy	95%				
Kappa Value	0.90				

Removal of basaltic talus points from the testing dataset increased the accuracy associated with our classification. This illustrated the constraints on the ability to separate a geomorphic signature of rhyolitic lava flows from those of basaltic talus or breccia. Talus and rhyolite on the seafloor had the same geomorphic signature in 1 m-resolution bathymetry because rhyolite commonly emplaces as either breccia or jagged flows in submarine environments [18–21,42]. When we removed two talus basalt samples in the testing data that were mis-classified as rhyolite, 100% of pixels classified as rhyolite were correct.

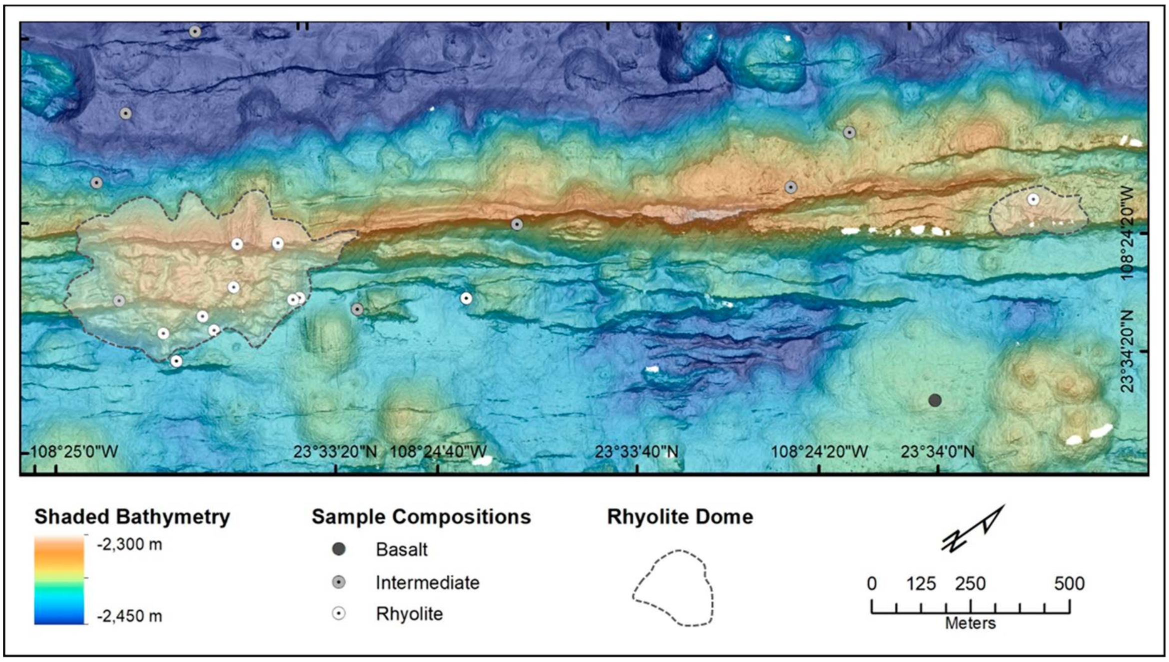

Figure 10. Map of testing data of 13 points reserved to test the classification accuracy for a rhyolitic geomorphic fingerprint, most on the main rhyolite dome, and one sample located at a smaller rhyolite dome to the north. Not all basaltic testing data are shown here.

8. Classification Results

To determine value ranges for the basaltic and rhyolitic classes, we compared the classified pixel value at each basalt and rhyolite sample location. The pixels were bi-modally distributed: basaltic samples clustered at the value of 0.9, and rhyolitic samples at 1.9; 75% of rhyolite and <3% of basalt were classified with values ≥1.7. Therefore, we defined the rhyolite class as including values ≥1.7. All pixels with values <1.7 were assigned to the basalt class (Figure 10). One of the benefits of fuzzy classification is the ability to manipulate the breaks between classification classes and test various scenarios to find those that apply in different areas on the basis of the testing data.

The resulting classification illustrates the distribution of lava flows with basaltic and rhyolitic geomorphic characteristics (Figure 11). ANFIS classified 94.5% of the Alarcon Rise as basalt (156 km^2 of seafloor). The remaining 5.5% was classified as rhyolite (9 km^2). The north ridge segment appeared to contain the majority of classified rhyolite, which is consistent with seafloor observations of rhyolite domes. ANFIS identified the ridge as mostly having a rhyolitic signature, including the rhyolite dome. Basalt was found to dominate the south ridge segment of the Alarcon Rise. Areas in this segment that ANFIS identified as rhyolitic appeared limited to the slopes of the larger volcanic cones [15] (Figure 12). Many pillows with high-to-intermediate silica content were classified as large basaltic pillows. Like submarine lava flows of intermediate composition observed elsewhere [13,14,27], the diameter and surficial striations of intermediate flows at the Alarcon Rise appeared to be larger and deeper than those of basaltic pillow lava (Figure 2). These are characteristics below the resolution of the sonar data in this study. Nevertheless, the number of samples assigned to the basaltic class increased with decreasing bulk silica content (Table 3).

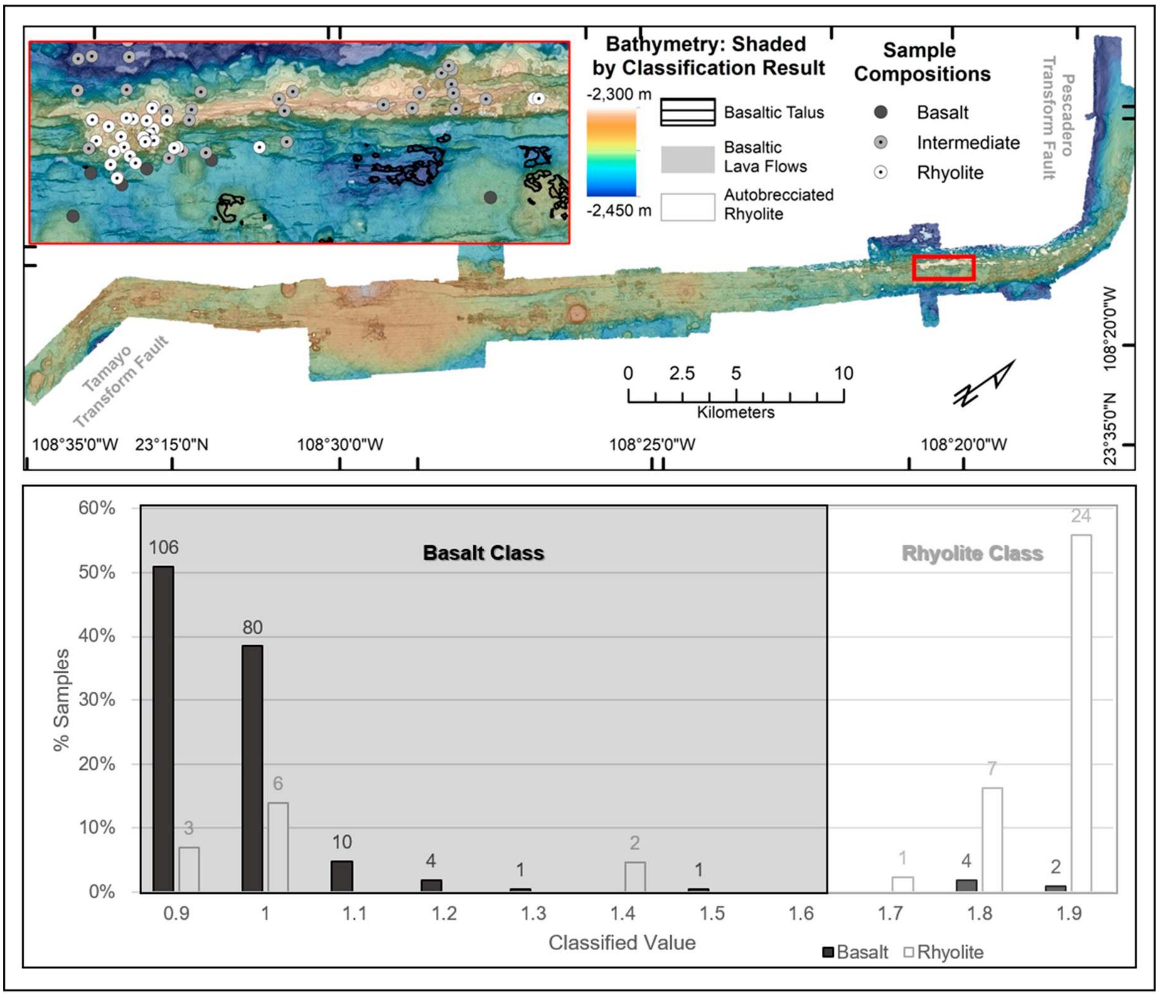

Figure 11. The vast majority of the Alarcon Rise was correctly classified as basaltic (light shading, top panel), with a rhyolitic signature (white outlines) dominantly in the north. Inset of the North AOI (red box) shows the majority of rhyolitic samples correctly classified with a rhyolitic fingerprint along with some intermediate samples classified as rhyolitic. The class break was chosen at a value of 1.7 because 75% of rhyolitic samples and only 3% of basaltic samples were classified with values equal to or above 1.7.

Table 3. Normalized percent of pixels assigned by classification for known sample lava composition.

Classification Results	Sample Composition				
	Basalt (208 Samples)	Basaltic Andesite (19 Samples)	Andesite (37 Samples)	Dacite (22 Samples)	Rhyolite (43 Samples)
% Basalt	97	89	76	73	26
% Rhyolite	3	11	24	27	74

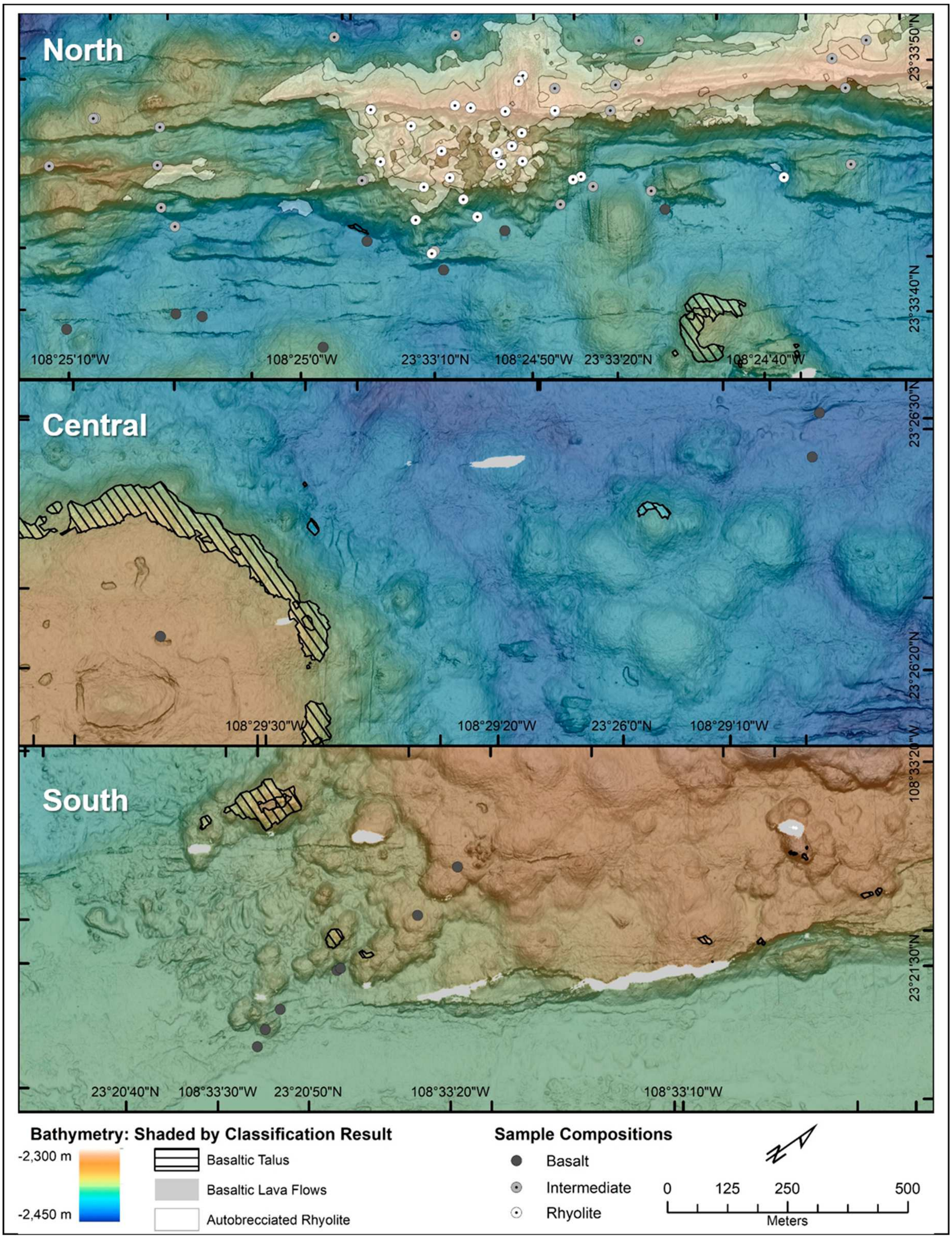

Figure 12. Classified map of the Alarcon Rise in three geomorphologic regions with testing data. The north region contains the majority of lava flows classified as rhyolite. The west side of the ridge also has a distinctly rhyolitic lava morphology compared to seafloor east of the ridge. The majority of the rhyolitic dome was classified with rhyolitic compositions. The central region was mostly classified as basalt. One notable exception is the edge of the volcanic cone. This is likely due to brecciated lava flows and talus at the steep sides. ANFIS correctly classified the southern lava shield as basaltic.

9. Discussion

This work shows that basalt flows can be distinguished in meter-scale bathymetry data from jagged rhyolites, and ANFIS classification can be used to distinguish these categories. Intermediate and basaltic pillow lava likely form similarly, but pillow diameter increases due to increased viscosity, slower effusion rate, and lower eruption temperature [43]. Intermediate-composition lava flows can exhibit a broad geomorphic range [28], yet intermediate-composition lava erupts in the submarine environment as large pillow flows mostly commonly [1–4,13,14]. Our interpretation of basaltic andesite, andesite, and dacite at the Alarcon Ridge is consistent with these observations (Figure 13).

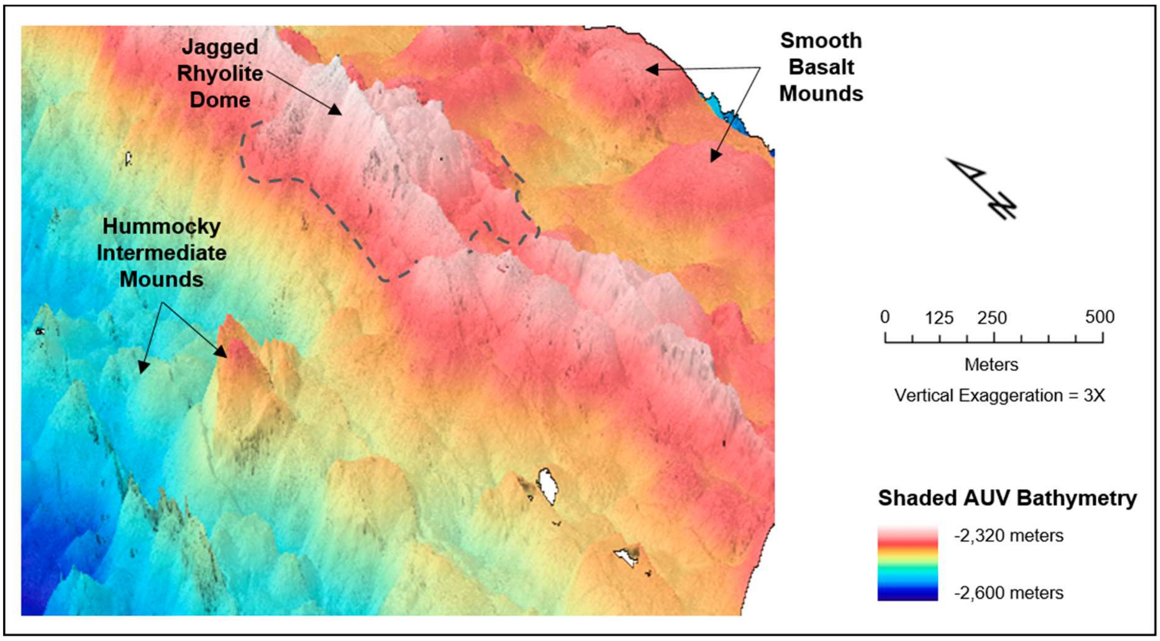

Figure 13. Intermediate-composition lava flows form hummocky mounds west of the north ridge at the Alarcon Rise. These mounds are similar in diameter to basaltic pillow mounds (100–200 m) but form rougher textures. We attribute the hummocks to the formation of large megapillows (>1 m diameter). Vertical exaggeration = 3×.

As the only known location of rhyolite erupted at an oceanic spreading ridge, the Alarcon Rise presents an unprecedented opportunity to address the way in which composition relates to lava morphology in an ocean rift zone environment (Figure 14). The most abrupt geomorphic change in this study was associated with dacitic to rhyolitic transition, when viscosity increased by 1–2 orders of magnitude [44]. Our results indicate that the formation of brecciated lava domes is characteristic of rhyolitic submarine lava flows. Rhyolite at the Alarcon Rise is emplaced as breccia, just as observed in other environments [18–21,42].

Our study revealed differences between rhyolitic and basaltic lava morphology at lava flow scale (10 m). We also initially experimented with backscatter and gray-level cooccurrene matrix (GLCM) textures using the 2012 side-scan sonar; however, coverage gaps at the rhyolite dome, sonar shadows, and lack of coverage relative to the 2015 multibeam data forced us to abandon the side-scan in this study to create a more comprehensive classification based over areas of suspected rhyolite. Incorporating both multibeam bathymetry and side-scan sonar backscatter datasets tends to improve the performance of the classifiers [32,45]. Incorporating sonar backscatter and GLCM textures may improve our classification results (e.g., [31,32,36,46,47]).

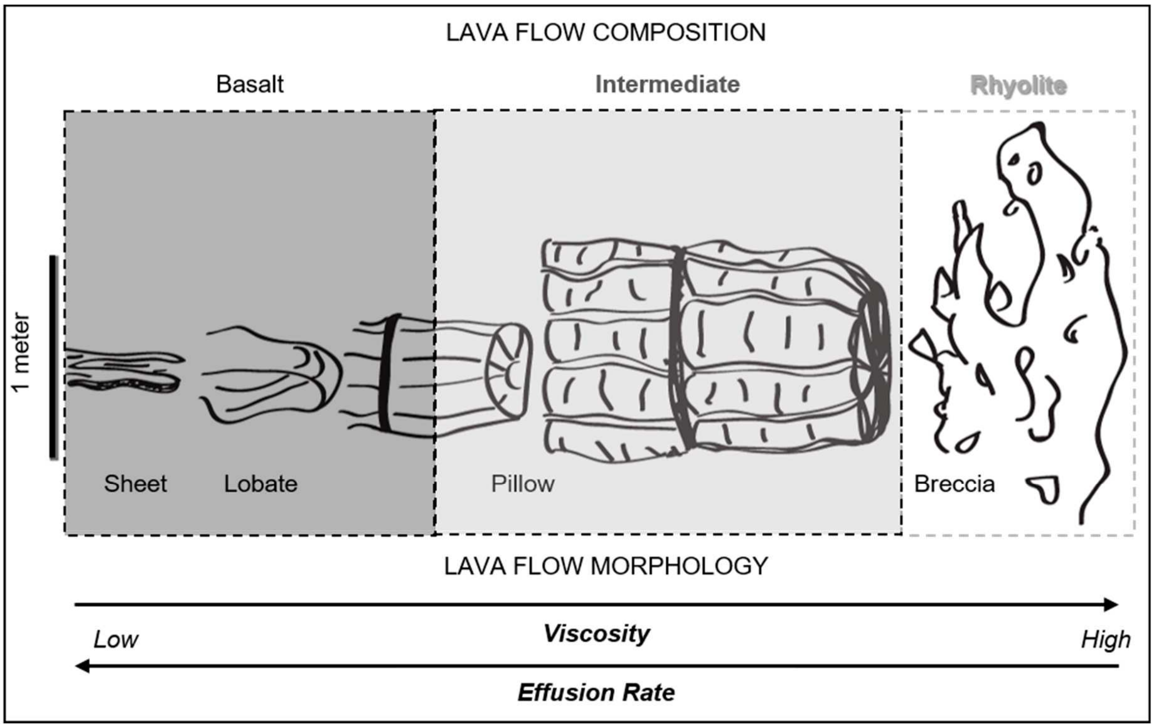

Figure 14. Changes in lava flow geomorphology and inferred emplacement processes with lava composition. Low-viscosity basaltic lava may erupt as sheet, lobate, or pillow morphologies depending on lava effusion rate. Lava flows with intermediate composition will emplace as pillows with diameters >1 m. The surfaces of these pillows will have striations ~10 cm deep, compared to basaltic pillows with striations ~1 cm deep. Rhyolitic lava flows will form jagged branches or may brecciate upon eruption.

Classifying geologic features at different scales is traditional practice in geomorphology (i.e., mound versus mountain). Investigation of the scale of different variables related to the composition of lava flows revealed underlying properties of the lava emplacement and thus proved to be a meaningful basis to construct the classification. For example, a scale of 100 m for the slope range rather than 10 m would have been trying to classify a completely different property than the wavelength of lava flow emplacement. Some scale-independent measures such as Bathy-morphons have been introduced recently [48], and future work should evaluate the morphon concept [49] for potential improvements to the ANFIS method.

The relationship between submarine lava flow geomorphology and lava composition also enhances our understanding of seafloor lava emplacement processes for a variety of compositions. Viscosity differences between basaltic and intermediate compositions can decrease the lava effusion rate. Slower moving lava would experience greater cooling and not be able to flow far on the seafloor under typical conditions, thus building hummocky pillow mounds [26]. Rhyolitic lava may emplace even slower than intermediate lava, creating brecciated domes such as the one found at the Alarcon Rise.

10. Conclusions

This study provides a first attempt at detecting and determining the spatial distribution of submarine lava flows with a rhyolite composition. In spite of visually observing only <0.5% of the seafloor along the axial zone, classification of the sonar map using ANFIS revealed approximately 95% of the seafloor at the Alarcon Rise is composed of sheet, lobate, or pillow lava flows, while rhyolite and talus account for 5%. The Alarcon Rise is a unique setting containing the broadest range of lava composition seen yet at a spreading ridge, so our results do not necessarily imply that rhyolite comprises 5% of all oceanic spreading ridges. This study shows that sonar-based classification is a useful first-order tool to identify rare high-silica submarine lava flows at oceanic spreading ridges and reveals universal relationships between lava composition and geomorphology.

Our study showed that geomorphic changes in submarine lava flows have thresholds related to composition and emplacement of flows (Figure 14). Basaltic lava yields a variety of lava geomorphologies ranging from sheet lava to pillow. This range contracts to only pillow morphology for intermediate compositions. Although basaltic andesite may form elongate or bulbous pillows, the diameter and depth of surficial striations increase in andesitic and dacitic lava flows. Despite the differences in flow scale for intermediate lava compositions, they remain a challenge to distinguish from basaltic pillows in 1 m gridded bathymetry. The most dramatic geomorphic threshold separates pillowed dacites from jagged rhyolites. Our classifier can identify areas on the seafloor that exhibit a jagged or brecciated texture but does not perform as well at distinguishing lava talus from the jagged-brecciated flows.

Author Contributions: Conceptualization, C.H.M. and S.M.W.; Methodology, C.H.M. and S.M.W.; Validation, all authors; Formal Analysis, C.H.M. supervised by S.M.W.; Investigation, C.H.M. and B.M.D.; Resources, D.A.C. and S.M.W.; Software, C.H.M. and S.M.W.; Data Curation, D.A.C.; Writing – Original Draft Preparation, C.H.M.; Writing – ReviewEditing, all authors; Visualization, C.H.M.; Supervision, S.M.W.; Project Administration, S.M.W. and D.A.C.; Funding Acquisition, S.M.W. and D.A.C.

Funding: The field data acquisiton and ship time was supported by the David and Lucile Packard Foundation through a grant to the Monterey Bay Aquarium Research Institute. B.M.D. was funded by U.S. National Science Foundation support from OCE-1355436 and OCE-1610800.

Acknowledgments: Processed MBARI AUV bathymetry is available at the IEDA Marine Geoscience Data System Repository at DOIs as follows 10.1594/IEDA/324366, 10.1594/IEDA/ 324367, 10.1594/IEDA/324368, and 10.1594/IEDA/324369. We are grateful to the Captains and crews of the R/V Western Flyer and Zepher, to the MBARI AUV team, the pilots of the MBARI ROV team, and the David and Lucile Packard Foundation for field support.

Conflicts of Interest: The authors declare no conflict of interest. The sponsors had no role in the design, execution, interpretation, or writing of the study.

References

1. Perfit, M.R.; Fornari, D.J. Geochemical studies of abyssal lavas recovered by DSRV *Alvin* from Eastern Galapagos Rift, Inca Transform, and Ecuador Rift 2. Phase chemistry and crystallization history. *J. Geophys. Res.* **1983**, *88*, 10530–10550. [CrossRef]
2. Perfit, M.R.; Fornari, D.J.; Malahoff, A.; Embley, R.W. Geochemical studies of abyssal lavas recovered by DSRV *Alvin* from Eastern Galapagos Rift, Inca Transform, and Ecuador Rift: 3. Trace element abundances and Petrogenesis. *J. Geophys. Res.* **1983**, *88*, 10551–10572. [CrossRef]
3. Regelous, M.; Niu, Y.; Wendt, J.I.; Batiza, R.; Greig, A.; Collerson, K.D. Variations in the geochemistry of magmatism on the East Pacific Rise at 10°30′ N since 800 ka. *Earth Planet. Sci. Lett.* **1999**, *168*, 45–63. [CrossRef]
4. Chadwick, J.; Perfit, M.; Ridley, I.; Jonasson, I.; Kamenov, G.; Chadwick, W.; Embley, R.; le Roux, P.; Smith, M. Magmatic effects of the Cobb hot spot on the Juan de Fuca Ridge. *J. Geophys. Res.* **2005**, *110*.
5. Gregg, T.K.; Fink, J.H. A laboratory investigation into the effects of slope on lava flow morphology. *J. Volcanol. Geotherm. Res.* **2000**, *96*, 145–159. [CrossRef]
6. McClinton, T.; White, S.M.; Colman, A.; Sinton, J.M. Reconstructing lava flow emplacement processes at the hot spot-affected Galápagos Spreading Center, 95° W and 92° W. *Geochem. Geophys. Geosyst.* **2013**, *14*, 2731–2756. [CrossRef]
7. Ballard, R.D.; Holcomb, R.T.; van Andel, T.H. The Galapagos Rift at 86° W: 3. Sheet flows, collapse pits, and lava lakes of the rift valley. *J. Geophys. Res.* **1979**, *84*, 5407–5422. [CrossRef]
8. Bonatti, E.; Harrison, C.G.A. Eruption styles of basalt in oceanic spreading ridges and seamounts: Effect of magma temperature and viscosity. *J. Geophys. Res. Solid Earth* **1988**, *93*, 2967–2980. [CrossRef]
9. Perfit, M.R.; Chadwick, W.W. Magmatism at Mid-Ocean Ridges: Constraints from Volcanological and Geochemical Investigations. *Geophys. Monogr.* **1998**, *106*, 59–115.

10. Kurras, G.J.; Fornari, D.J.; Edwards, M.H.; Perfit, M.R.; Smith, M.C. Volcanic morphology of the East Pacific Rise Crest 9°49′–52′: Implications for volcanic emplacement processes at fast-spreading mid-ocean ridges. *Mar. Geophys. Res.* **2000**, *21*, 23–41. [CrossRef]
11. Cann, J.R.; Smith, D.K. Evolution of volcanism and faulting in a segment of the Mid-Atlantic Ridge at 25° N. *Geochem. Geophys. Geosyst.* **2005**, *6*, 1–20. [CrossRef]
12. Fundis, A.T.; Soule, S.A.; Fornari, D.J.; Perfit, M.R. Paving the seafloor: Volcanic emplacement processes during the 2005-2006 eruptions at the fast spreading East Pacific Rise, 9°50′ N. *Geochem. Geophys. Geosyst.* **2010**, *11*, Q08024. [CrossRef]
13. Wanless, V.D.; Perfit, M.R.; Ridley, W.I.; Klein, E. Dacite petrogenesis on mid-ocean ridges: Evidence for oceanic crustal melting and assimilation. *J. Petrol.* **2010**, *51*, 2377–2410. [CrossRef]
14. Stakes, D.S.; Perfit, M.R.; Tivey, M.A.; Caress, D.W.; Ramirez, T.M.; Maher, N. The Cleft revealed: Geologic, magnetic, and morphologic evidence for construction of upper oceanic crust along the southern Juan de Fuca Ridge. *Geochem. Geophys. Geosyst.* **2006**, *7*. [CrossRef]
15. Clague, D.A.; Caress, D.W.; Dreyer, B.M.; Lundsten, L.; Paduan, J.B.; Portner, R.A.; Le Saout, M. Geology of the Alarcon Rise, Southern Gulf of California. *Geochem. Geophys. Geosyst.* **2018**, *19*, 807–837. [CrossRef]
16. Gregg, T.K.P.; Fink, J.H. Quantification of submarine lava-flow morphology through analog experiments. *Geology* **1995**, *23*, 73–76. [CrossRef]
17. Fiske, R.S.; Naka, J.; Iizasa, K.; Yuasa, M.; Klaus, A. Submarine silicic caldera at the front of the Izu-Bonin arc, Japan: Voluminous seafloor eruptions of rhyolitic pumice. *GSA Bull.* **2001**, *113*, 813–824. [CrossRef]
18. Goto, Y.; Tsuchiya, N. Morphology and growth style of a Miocene submarine dacite lava dome at Atsumi, northeast Japan. *J. Volcanol. Geotherm. Res.* **2004**, *134*, 255–275. [CrossRef]
19. Honsho, C.; Ura, T.; Kim, K.; Asada, A. Postcaldera volcanism and hydrothermal activity revealed by autonomous underwater vehicle surveys in Myojin Knoll caldera, Izu-Ogasawara arc. *J. Geophys. Res. Solid Earth* **2016**, *121*, 4085–4102. [CrossRef]
20. Scutter, C.R.; Cas, R.A.F.; Moore, C.L. Facies architecture and origin of a submarine rhyolitic lava flow-dome complex, Ponza, Italy. *J. Geophys. Res.* **1998**, *103*, 27551–27556. [CrossRef]
21. DeRita, D.; Giordano, G.; Cecili, A. A model for submarine rhyolite dome growth: Ponza Island (central Italy). *J. Volcanol. Geotherm. Res.* **2001**, *107*, 221–239. [CrossRef]
22. Chadwick, W.W.; Scheirer, D.S.; Embley, R.W.; Johnson, P. High-resolution bathymetric surveys using scanning sonars: Lava flow morphology, hydrothermal vents, and geologic structure at recent eruption sites on the Juan de Fuca Ridge. *J. Geophys. Res.* **2001**, *106*, 16075–16099. [CrossRef]
23. Caress, D.W.; Paduan, J.; Clague, D.A.; Spelz-Madero, R. Processed Gridded Near-Bottom Bathymetry Data (ArcASCII fomat) from the Alarcon Rise Spreading Center, Integrated Earth Data Alliance (IEDA). 2018. Available online: http://get.iedadata.org/doi/324367 (accessed on 30 March 2019).
24. Caress, D.W.; Thomas, H.; Kirkwood, W.J.; McEwen, R.; Henthorn, R.; Clague, D.A.; Paull, C.K.; Paduan, J.; Maier, K.L. High-resolution multibeam, sidescan, and subbottom surveys using the MBARI AUV *D. Allan B*. In *Marine Habitat Mapping Technology for Alaska*; Reynolds, J.R., Greene, H.G., Eds.; University of Alaska: Colitch, AK, USA, 2008; pp. 47–69.
25. Fisher, A.T.; Giambalvo, E.; Sclater, J.; Kastner, M.; Ransom, B.; Weinstein, Y.; Lonsdale, P. Heat flow, sediment and pore fluid chemistry, and hydrothermal circulation on the east flank of Alarcon Ridge, Gulf of California. *Earth Planet. Sci. Lett.* **2001**, *188*, 521–534. [CrossRef]
26. Yeo, I.; Searle, R.C.; Achenbach, K.L.; Le Bas, T.P.; Murton, B.J. Eruptive hummocks: Building blocks of the upper ocean crust. *Geology* **2012**, *40*, 91–94. [CrossRef]
27. Mills, S.R.; Perfit, M.; Clague, D.A.; Paduan, J.B. Petrology and petrogenesis of andesites from Axial Seamount, Juan de Fuca Ridge, Geological Society of America, Cordilleran Section. In Proceedings of the 113th Annual Meeting, Honolulu, HI, USA, 23–25 May 2017; p. 44.
28. Embley, R.W.; Rubin, K.H. Extensive young silicic volcanism produces large deep submarine lava flows in the NE Lau Basin. *Bull. Volcanol.* **2018**, *80*, 36. [CrossRef]
29. Batiza, R.; Smith, T.L.; Niu, Y. Geological and petrologic evolution of seamounts near the EPR based on submersible and camera study. *Mar. Geophys. Res.* **1989**, *11*, 169–236.
30. Gregg, T.K.; Smith, D.K. Volcanic investigations of the Puna Ridge, Hawai′ i: Relations of lava flow morphologies and underlying slopes. *J. Volcanol. Geotherm. Res.* **2003**, *126*, 63–77. [CrossRef]

31. Meyer, J.D.; White, S.M. Lava morphology mapping by expert system classification of high-resolution side-scan sonar imagery from the East Pacific Rise, 9°–10° N. *Mar. Geophys. Res.* **2007**, *28*, 81–93. [CrossRef]
32. McClinton, J.T.; White, S.M.; Sinton, J.M. Neuro-fuzzy classification of submarine lava flow morphology. *Photogramm. Eng. Sens.* **2012**, *78*, 605–616. [CrossRef]
33. Horn, B.K. Hill shading and the reflectance map. *Proc. IEEE* **1981**, *69*, 14–47. [CrossRef]
34. Lundbald, E.R.; Wright, D.J.; Miller, J.; Larkin, E.M.; Rinehart, R.; Naar, D.F.; Donahue, B.T.; Anderson, S.M.; Battista, T. A benthic terrain classification scheme for American Samoa. *Mar. Geod.* **2006**, *29*, 89–111. [CrossRef]
35. Stewart, K.; Jiang, M.; Marra, M. A neural network approach to classification of sidescan sonar imagery from a midocean ridge area. *IEEE J. Ocean. Eng.* **1994**, *19*, 214–224. [CrossRef]
36. Blondel, P. Segmentation of the Mid-Atlantic Ridge south of the Azores, based on acoustic classification of TOBI data. *Geol. Soc. Spec. Publ.* **1996**, *118*, 1–13. [CrossRef]
37. Gao, D.; Hurst, S.; Karson, J.; Delaney, J.; Spiess, F. Computer-aided interpretation of side-looking sonar images from the eastern intersection of the Mid-Atlantic Ridge with the Kane Transform. *J. Geophys. Res.* **1998**, *103*, 20997–21014. [CrossRef]
38. Jang, J.R. ANFIS: Adaptive-network-based fuzzy inference system. *IEEE Trans. Syst. Man Cybern.* **1993**, *23*, 665–685. [CrossRef]
39. Zadeh, L.A. Fuzzy sets. *Inf. Control* **1965**, *8*, 338–353. [CrossRef]
40. Congalton, R.G. A review of assessing the accuracy of classifications of remotely sensed data. *Remote Sens. Environ.* **1991**, *37*, 35–46. [CrossRef]
41. Landis, J.R.; Koch, G.G. The measurement of observer agreement for categorical data. *Biometrics* **1977**, *33*, 159–174. [CrossRef]
42. Yamagishi, H.; Dimroth, E. A comparison of Miocene and Archean rhyolite hyaloclastites: Evidence for a hot and fluid rhyolite lava. *J. Volcanol. Geotherm. Res.* **1985**, *23*, 337–355. [CrossRef]
43. Stasiuk, M.V.; Jaupart, C. Lava flow shapes and dimensions as reflections of magma system conditions. *J. Volcanol. Geotherm. Res.* **1997**, *78*, 31–50. [CrossRef]
44. Whittington, A.G.; Hellwig, B.M.; Behrens, H.; Joachim, B.; Stechern, A.; Vetere, F. The viscosity of hydrous dacitic liquids: Implications for the rheology of evolving silicic magmas. *Bull. Volcanol.* **2009**, *71*, 185–199. [CrossRef]
45. Diesing, M.; Mitchell, P.; Stephens, D. Image-based seabed classification: What can we learn from terrestrial remote sensing? *ICES J. Mar. Sci.* **2016**, *73*, 2425–2441. [CrossRef]
46. Lucieer, V.L. Object-oriented classification of sidescan sonar data for mapping benthic marine habitats. *Int. J. Remote Sens.* **2008**, *29*, 905–921. [CrossRef]
47. Reed, T.B.; Hussong, D. Digital Image Processing Techniques for Enhancement and Classification of SeaMARC II Side Scan Sonar Imagery. *J. Geophys. Res. Solid Earth* **1989**, *94*, 7469–7490. [CrossRef]
48. Masetti, G.; Mayer, L.A.; Ward, L.G. A bathymetry-and reflectivity-based approach for seafloor segmentation. *Geosciences* **2018**, *8*, 14. [CrossRef]
49. Jasiewicz, J.; Stepinski, T.F. Geomorphons—A pattern recognition approach to classification and mapping of landforms. *Geomorphology* **2013**, *182*, 147–156. [CrossRef]